Icarus 220 (2012) 383–391

Contents lists available at SciVerse ScienceDirect

Icarus

journal homepage: www.elsevier.com/locate/icarus

Collisional features in a model of a planetary ring

Brian P. Lawney [a,*], James T. Jenkins [b], Joseph A. Burns [a]

[a] Field of Theoretical and Applied Mechanics, Sibley School of Mechanical Engineering, Cornell University, Ithaca, NY 14853, United States
[b] Field of Theoretical and Applied Mechanics, School of Civil and Environmental Engineering, Cornell University, Ithaca, NY 14853, United States

ARTICLE INFO

Article history:
Received 3 August 2011
Revised 29 April 2012
Accepted 6 May 2012
Available online 23 May 2012

Keywords:
Collisional physics
Planetary rings
Saturn, Rings

ABSTRACT

Images taken by the Cassini spacecraft display numerous "propellers", telltale disturbances detected in Saturn's outer A ring. In conventionally accepted models (Seiß, M., Spahn, F., Sremčević, M., Salo, H. [2005]. Geophys. Res. Lett. 32, L11205; Lewis, M., Stewart, G. [2009]. Icarus 199, 387–412), unseen moonlets are considered to generate these structures by gravitationally stirring the shearing Kepler flow of ring particles. The morphology and scale of these structures likely depend on both gravity and collisions. However, with a goal to understand one aspect of the development of real propellers, and motivated by similar features observed in terrestrial granular systems, we here study only the collisional effects on propeller-like feature formation, entirely omitting the gravitational attraction between the moonlet and the particles.

Our investigation employs a combination of simulation and continuum analysis to examine the extent to which dissipative collisions between ring particles and with a large obstacle might cause such features to form. Our simple, heuristic two-dimensional numerical simulations demonstrate that propeller-like features having many of the features seen in gravitating systems can form. Our continuum theory predicts that, at observed ring densities, the magnitudes of relative particle speeds and thermal speeds (i.e., kinetic granular temperatures) imply that the flow with respect to the moonlet is supersonic. As a consequence, these propeller-like features could be interpreted as the locus of a granular shock across which the flow experiences significant, almost discontinuous, changes in flow properties.

1. Introduction

Among Cassini's major discoveries in the Saturn system is a population of ring features (Tiscareno et al., 2006), so-called "propellers," that has been detected in the outer A ring and perhaps elsewhere (Sremčević et al., 2011). These pairs of (bright or dark) streaks lie along the orbital direction and are slightly offset radially. Such features are attributed to small unseen moonlets that gravitationally perturb typical ring particles as they pass by in a Keplerian shear flow (Spahn and Sremčević, 2000; Seiß et al., 2005; Lewis and Stewart, 2009). They thus share properties with protoplanets that are believed to have resided in the early solar nebula, hence the interest in them and their orbital behavior.

Since the causative moonlets for the propellers cannot be resolved in the Cassini spacecraft images, models then become crucial to infer indirectly the moonlet's mass; as described later, such models generally find that the moonlet's Hill spheres are proportional to the separation between the arms of the visible disturbance in the ring material. On this basis, the unseen moonlets range in radius from ~10 m to perhaps 1 km and display a steep size distribution, $q \sim 6$, where the differential number of particles of radius r is $n(r) \sim r^{-q}$ (Tiscareno et al., 2006, 2008). According to these ideas, when the embedded masses become large enough, the propeller features extend entirely around the planet so that complete gaps are opened in the rings; the ring moons Pan and Daphnis, which inhabit the Encke and Keeler gaps, respectively, fit into this picture quite well (cf. Cuzzi et al., 2010). The provenance of the largest ring masses is open to current debate, but it is agreed that their precise size distribution, as inferred by the gravitational models, must furnish clues about the origin of the rings themselves (Charnoz et al., 2009).

Saturn's rings are composed of innumerable water–ice particles that orbit the central planet in a thin sheet. The particles in the classical A, B and C rings form a power–law size distribution ranging from 10^{-2} m to ~10 m, according to radio observations taken by Voyager three decades ago (Zebker et al., 1985; Cuzzi et al., 2009). In most ring regions, large fractions of ring surface area are completely covered, implying that a typical ring particle frequently collides with others during each orbit of the planet.

The model that we will present below will, for simplicity, take the ring to be two-dimensional. The vertical thickness of Saturn's rings – specifically the question of the extent to which planetary rings form monolayers – received considerable theoretical and

* Corresponding author.
E-mail address: brianlawney@gmail.com (B.P. Lawney).

0019-1035/$ - see front matter © 2012 Elsevier Inc. All rights reserved.
http://dx.doi.org/10.1016/j.icarus.2012.05.011

observational attention in the Voyager era. That interest continues today (see reviews by Cuzzi et al. (2009, 2010) and Schmidt et al. (2009)): Cassini observations of stellar and radio occultations across ring perimeters suggest ring thicknesses, which may also be inferred from the properties of spiral density waves and the nature of the transmitted signal in radio occultations through the ring proper. These results indicate that most regions of Saturn's rings are 10 m to tens of meters thick, i.e., at most a few times the size of the largest ring particles in a typical power–law size distribution. Many have interpreted these measurements to confirm simple theoretical arguments and simulations that indicate an orbiting swarm of single-size, lossy particles will collapse rapidly to deposit all particles within a few particle diameters of the planet's equatorial plane. Thus classical radio-transmission models (e.g., Zebker et al., 1985) are based on thin layers. In systems containing a particle size distribution, the smallest particles will reside in a layer that is many small particles thick (Cuzzi et al., 1979), but still only a few large particles thick. The general belief (but one that cannot yet be confirmed) among Cassini scientists is that, in the densest part of Saturn's rings, the most massive ring particles lie roughly in a monolayer.

In any case, because our goal in this paper is a heuristic one, namely to address in a novel way the fundamental role that collisions play in producing propeller-like features in shear flow (or to open insights into a different fashion to think about propeller formation), we will investigate a two-dimensional model. Such a model allows easier interpretation and permits a more complete analysis.

To put our simple investigation into context, we here review past theoretical and numerical studies of propeller formation. Spahn and Sremčević (2000) applied a viscous continuum model to numerically examine density disturbances due to a perturbing body. In their two-dimensional treatment, the system has two parts – a scattering region and a mean (shearing) Keplerian flow. The gravitational influence of the moonlet is restricted to a line at the moonlet's azimuthal location and the scattering is modeled as a Markov process. The flux of scattered particles provides a boundary condition for the viscous transport to the mean flow. Sremčević et al. (2002) also employed this model, using Green's functions to solve the diffusion-type boundary-value problem. Both studies considered energetic effects to be of minor importance compared to mass and momentum transport. Later, Seiß et al. (2005) conducted three-dimensional *N*-body simulations of uniform, inelastic particles with a restitution coefficient of $e = 0.5$. They found the azimuthal-averaged optical depth of the propellers scaled well with the Hill radius (Murray and Dermott, 1999) in the radial direction and the azimuthal extent of the features correlated with moonlet mass and ring viscosity. It is worth noting that scaling laws have been confirmed by some (Sremčević et al., 2007) and not by others (Tiscareno et al., 2008).

Lewis and Stewart (2009) increased the complexity of these numerical studies, employing a three-dimensional, *N*-body simulation that included both particle size distributions and self-gravity. As well as investigating these additional effects on propeller formation, they examined particle clustering about the moonlet and accretion in the shearing flow. Michikoshi and Kokubo (2011) numerically simulated the development of propellers in regions of very high surface density to ascertain the extent to which the presence of self-gravity wakes might impede propeller formation. They found that propellers formed as long as the wavelength of the gravitational wakes was less than the moonlet's Hill radius; this condition is satisfied throughout the A ring.

A feature common to all prior work has been the inclusion of the moonlet as a gravitational mass. No previous study has examined this problem in the absence of moonlet gravity. Instead, we will create a purely collisional system under the influence of only the gravitational forces that drive the shearing flow. We are not arguing against the importance of moonlet and self-gravitational effects in any realistic model. Rather, for heuristic purposes, we wish to present a different perspective to help readers understand the roles of different processes in propeller formation. As a consequence of this different perspective, previous interpretations of simulation results and current size-scaling laws may require some reconsideration.

Filamentary density concentrations are commonly found in terrestrial granular flows where gravitational attraction has no role (see the numerical simulations of Hopkins and Louge (1991)). An everyday example illustrates this point: in vehicular traffic, congestion begets further congestion (auto collisions even more so!). By analogy, the expectation is that when ring particles – driven by Keplerian shear – crash into a moonlet and rebound inelastically, the region close to the moonlet will become clogged with ring material. Indeed, similar to supersonic compressible gases, granular systems can also experience spatial changes in their properties (shocks) when the flow speed exceeds that of the sound speed in the material. If information about the presence of obstructing bodies (as realized through collisions) cannot be transmitted upstream, the flow does not alter its properties smoothly to accommodate for the body; thus a shock develops. Granular shocks have been investigated in simple geometries both experimentally (Rericha et al., 2002; Gray and Cui, 2007) and numerically (Rericha et al., 2002), but only limited analytical work has been performed (Gray and Cui, 2007; Haff, 1983), especially for dense-gas treatments.

Using an adapted kinetic theory for plane flows of inelastic, frictionless disks (Jenkins and Richman, 1985, 1988), in Section 2 we derive an expression for the strength of the velocity fluctuations (granular temperature) in shear flow. Following this, we employ elements of equilibrium thermodynamics to arrive at a relation for the sound speed as a function of this temperature and solid fraction. We show that for intermediate planar densities (e.g. 30–70%), incident flows upon the moonlet are predominantly supersonic; accordingly, we suggest that the propeller-like feature observed may represent the locus of a detached bow shock. We support our analysis by simple two-dimensional *N*-body simulations (Sections 3 and 4) of a Keplerian shearing flow past an obstacle, investigating the effects of relative obstacle size, density (fractional area coverage), and collision inelasticity on the nature of the structures produced.

The simulations that we describe are *not* intended to compete with existing three-dimensional simulations (e.g., Lewis and Stewart, 2009; Michikoshi and Kokubo, 2011) in terms of realism. They are meant to be the simplest that capture the collisional interactions in a shear flow and indicate how these alone may lead to propeller-like features around an obstructing body. We do not intend to minimize the potential importance of gravitational interactions to the formation of propellers in realistic ring models. Our intent is to show instead in the simplest possible context that such interactions are not fundamental for the development of propeller-like features.

2. Analysis

According to our model, a general particle experiences no gravitational forces from the moonlet nor from other companion particles. Hence, the observed formation of any density structures in our simulations can only be due to the interparticle collisions and orbital dynamics in the moonlet frame (as described by Hill's equations – see Section 3). We adopt a modified two-dimensional kinetic theory for the plane flow of inelastic, smooth disks and elements of equilibrium thermodynamics to show that at observed

densities and strength of the velocity fluctuations (granular temperature), the Keplerian flow with respect to the moonlet is predominantly supersonic. Because of this, we interpret the propeller-shaped density features that we observe about moonlets as granular shock fronts.

In contrast to the dilute, three-dimensional ring considered, for example, by Goldreich and Tremaine (1978), we consider a dense two-dimensional flow where the increased frequency of collisions reduces or eliminates the anisotropy in the dispersion velocity. Consequently, the appropriate analysis for our dense "ring" is more like that of granular kinetic theory that involves an isotropic temperature determined by an energy balance.

Salo (1995) and Daisaka and Ida (1999) have shown that dense rings possess inhomogeneous structure (wakes) due to inelastic collisions and mutual gravitation which indeed produces complicated variations with space and time in the particle velocity distribution, but we do not consider this in our treatment. Depending upon ring conditions (e.g., optical depth and collisional dissipation) such structure may be more or less important in a given model, but it is not yet clear that these wakes would preclude our "propellers" from providing insight to the role of collisions in more realistic treatments. Various regions of Saturn's rings, such as its C ring, better satisfy the conditions that our model assumes.

2.1. Granular temperature in shear flow

We next compute the velocity dispersion of identical, inelastic, circular disks of diameter d in two-dimensional dense, steady shear. We will use this result to show that non-gravitating flows with planar densities similar to that of rings have a relatively low mean agitation with respect to the flow speed and, thus, disturbance information is slow to propagate through the medium.

We first examine the energy-balance equation (Jenkins and Richman, 1985),

$$\rho\dot{T} + P_{\alpha\beta}D_{\alpha\beta} + \frac{\partial q_\alpha}{\partial x_\alpha} = \Gamma, \tag{1}$$

where ρ is the surface mass density, T the granular temperature, $\mathbf{P}$ the pressure tensor, $\mathbf{D}$ the rate of strain tensor, $\nabla\cdot\mathbf{q}$ the divergence of the heat flux, and Γ the rate of collisional energy dissipation. Greek subscripts denote components with respect to orthogonal basis vectors in the plane and we sum over repeated indices. Given an ensemble mean velocity $\mathbf{u}\equiv\langle\mathbf{c}\rangle$, the fluctuating velocity component is $\mathbf{C}=\mathbf{c}-\mathbf{u}$, and the granular temperature in two dimensions is $T\equiv\langle\mathbf{C}\cdot\mathbf{C}\rangle$. The surface mass density is the product of the constituent material's density ρ_m and the area fraction ν. For a number density n, the area fraction is defined as $\nu=n\pi d^2/4$.

In steady state, the adiabatic energy equation ($\nabla\cdot\mathbf{q}=0$) simplifies to

$$P_{\alpha\beta}D_{\alpha\beta} = \Gamma, \tag{2}$$

which expresses the balance of stress-work and collisional dissipation. With $D_{\alpha\beta}\equiv(u_{\alpha,\beta}+u_{\beta,\alpha})/2$, the only non-trivial component in the shear flow is $D_{xy}=D_{yx}=\dot\gamma/2$, where $\dot\gamma\equiv\partial u/\partial y$ is the shear rate (coordinate y is defined in Fig. 4). Owing to the symmetry of the pressure tensor, we may write

$$P_{xy}\dot\gamma = \Gamma. \tag{3}$$

The rate of collisional dissipation for frictionless disks with restitution coefficient e is (Jenkins and Richman, 1985)

$$\Gamma = -\frac{4\alpha T(1-e)}{d^2}, \tag{4}$$

where $\alpha\equiv 8m\nu^2 g_0\breve{r}T^{\frac{1}{2}}/d\pi^{\frac{3}{2}}$ is the bulk viscosity, m is the disk's mass, $\breve{r}\equiv(1+e)/2$, and

$$g_0(\nu) = \frac{16-7\nu}{16(1-\nu)^2} \tag{5}$$

is the radial distribution function for disks in contact (Verlet and Levesque, 1982). Additionally, we define $G\equiv\nu g_0$.

The pressure tensor is

$$P_{\alpha\beta} = (p-\alpha D_{\gamma\gamma})\delta_{\alpha\beta} - 2\mu D_{\alpha\beta}. \tag{6}$$

The isotropic pressure is given by the equation of state,

$$p = \rho(1+2G\breve{r})T \tag{7}$$

and the viscosity (Jenkins and Richman, 1985) is

$$\mu = \mu'(1+G\breve{r}) + \frac{\alpha}{2}, \tag{8}$$

where

$$\mu' = \frac{m\nu T^{1/2}}{Gd(5-3\breve{r})\sqrt{\pi}}[1+G\breve{r}(3\breve{r}-2)]. \tag{9}$$

The shear stress is, then,

$$P_{xy} = \frac{-m\nu T^{1/2}\dot\gamma}{Gd\sqrt{\pi}(5-3\breve{r})}[1-G\breve{r}+(3G-2G^2)\breve{r}^2+3G^2\breve{r}^3] - \frac{\alpha\dot\gamma}{2}. \tag{10}$$

Eqs. (4) and (10) used in the energy equation yield an expression for $T^*\equiv T/d^2\dot\gamma^2$:

$$T^* = \frac{1}{16(1-\breve{r})}\left[\frac{\pi[1-G\breve{r}+(3G-2G^2)\breve{r}^2+3G^2\breve{r}^3]}{4G^2\breve{r}(5-3\breve{r})}+1\right]. \tag{11}$$

Eq. (11) is plotted for several restitution coefficients in Fig. 1. Note that as the area fraction increases we expect increased collision frequency which, in turn, decreases the velocity fluctuations about the mean. Lowering the restitution coefficient has a similar effect, as fluctuations are damped further by the more dissipative collisions.

We note that the nature of these curves agrees with the numerical findings of Walton and Braun (1986) who measured the granular temperature for shearing flows of dissipative, frictional disks.

2.2. Speed of sound

By definition (Anderson, 2000), the speed of sound, a, in a material is

$$a^2 = \left(\frac{\partial p}{\partial\rho}\right)_s = \frac{1}{\rho_s}\left(\frac{\partial p}{\partial\nu}\right)_s, \tag{12}$$

where the partial derivatives are taken with entropy s held fixed – an isentropic process. The isentropic sound speed is certainly an approximate measure since it does not incorporate the collisional

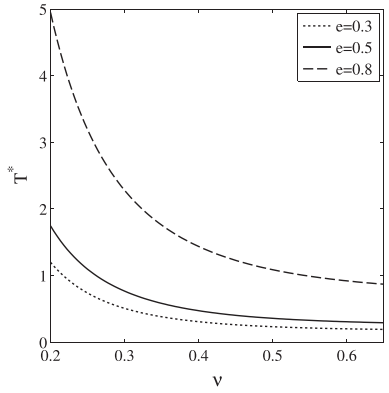

Fig. 1. Non-dimensional temperature $T^*=T/(d\dot\gamma)^2$ versus area fraction. Eq. (11) is plotted for restitution coefficients of $e=0.3$, 0.5, 0.8.

dissipation (i.e. here $\breve{r} = 1$). However, this provides an upper limit, as inelastic collisions would only decrease the sound speed. In thermodynamic equilibrium, the general expression for the sound speed is (Anderson, 2000)

$$a^2 = \frac{1}{\rho_s}\left(\frac{\partial p}{\partial v}\right)_s = \frac{\left[\left(\frac{\partial h}{\partial v}\right)_T\left(\frac{\partial v}{\partial T}\right)_p + \left(\frac{\partial h}{\partial T}\right)_v\right]\left[\rho_s v^2\left(\frac{\partial \phi}{\partial v}\right)_T - p\right]}{\rho_s\left[\rho_s v^2\left(\frac{\partial h}{\partial v}\right)_T\left(\frac{\partial v}{\partial p}\right)_T - v\right]\left(\frac{\partial \phi}{\partial T}\right)_v}, \tag{13}$$

where $\phi(v,T)$ is the internal energy per unit mass and $h = \phi + p/(\rho_s v)$ is the enthalpy. For hard disks in two dimensions, ϕ is strictly a function of the temperature: $\phi(T) = T$. Additionally, for planar flow of uniform disks, an equation of state relates the particle pressure p and temperature:

$$p = \rho_s v[1 + 2G(v)]T = \rho_s v\left(\frac{v^2+8}{8(1-v)^2}\right)T. \tag{14}$$

Because we can express any thermodynamic potential as a function of two state variables, we choose these to be v and T, and write the enthalpy as

$$h(v,T) = T + \frac{v^2+8}{8(1-v)^2}T, \tag{15}$$

Upon substituting this expression in Eq. (13), we obtain the temperature-normalized sound speed in terms of the area fraction:

$$\frac{a^2}{T} = \frac{9v^4 - 32v^3 - 24v^2 + 128}{64(1-v)^4}. \tag{16}$$

In Fig. 2 we plot Eq. (16) along with the dilute limit where $G(v) \ll 1$ and the sound speed becomes strictly a function of the temperature $a_d \sim \sqrt{T}$ as in a perfect gas. We observe that as the density increases we have a greater sound speed due to the higher collision frequency.

2.3. Mach number

With expressions (11) and (16) for the temperature and sound speed, respectively, we specify the Mach number, $M = u/a$, as the ratio of flow speed to sound speed; then $M = 1$ defines the transition from subsonic ($M < 1$) to supersonic ($M > 1$). In Keplerian flow with a shear rate $\dot{\gamma}$, we may write the azimuthal speed as a function of the radial distance y from the moonlet's azimuthal axis. Defining the dimensionless distance $y^* \equiv y/d$, we have

$$u = \dot{\gamma} y^* d. \tag{17}$$

We use this in the expression for the temperature from Eq. (11), and eliminate any dependence upon d and $\dot{\gamma}$:

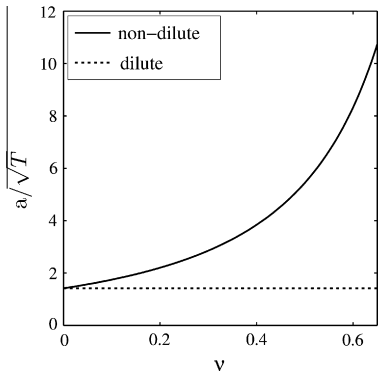

Fig. 2. Variation of normalized sound speed, a, with area fraction for $v = [0.0\ 0.65]$. The dilute limit a_d which has no density dependence is plotted for comparison.

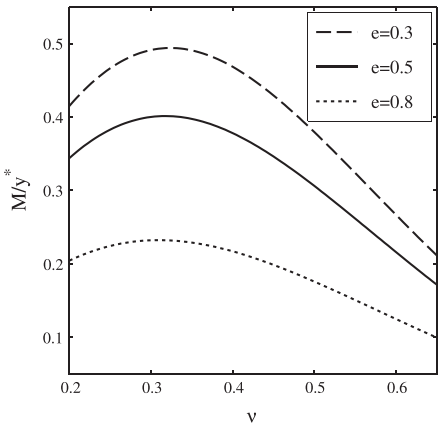

Fig. 3. Mach number M divided by dimensionless radial displacement y^*. Restitution coefficient values of $e = 0.3, 0.5, 0.8$ are chosen for area fractions v between 0.2 and 0.65.

$$\frac{u^2}{T} = \frac{64G^2 y^{*2}(5\breve{r} - 8\breve{r}^2 + 3\breve{r}^3)}{\left[\pi + (20G^2 - G\pi)\breve{r} + (3\pi G - 2\pi G^2 - 12G^2)\breve{r}^2 + 3\pi G^2\breve{r}^3\right]}. \tag{18}$$

Thus, we may divide by (16) and write the square of the Mach number as,

$$M^2 = \frac{4096G^2 y^{*2}(5\breve{r} - 8\breve{r}^2 + 3\breve{r}^3)(1-v)^4}{\varsigma(v)[\pi + (20G^2 - G\pi)\breve{r} + (3\pi G - 2\pi G^2 - 12G^2)\breve{r}^2 + 3\pi G^2\breve{r}^3]}, \tag{19}$$

where

$$\varsigma(v) = 9v^4 - 32v^3 - 24v^2 + 128. \tag{20}$$

The Mach number can thus be expressed as a function of restitution coefficient, area fraction, and the radial distance from the moonlet's semi-major axis; see Fig. 3.

The qualitative shape of the curves in Fig. 3 is due to the competing effects of the temperature and sound speed in the shear flow, as shown previously in Figs. 1 and 2. At dilute area fractions, the flow has a relatively low sound speed due to less frequent collisions, but the granular temperature is accordingly higher. Conversely, denser area fractions yield higher sound speeds through increased collisions, which serve to lower the temperature.

3. Simulation

To model the problem numerically, a two-dimensional N-body simulation of identical, frictionless, circular disks was developed, ignoring any moonlet and interparticle gravitation. We fix the origin of a translating and rotating reference frame to a moonlet of diameter D, which moves on a circular orbit at a distance R from a central gravitating body (e.g., Saturn). In our local coordinate system, the positive radial direction y is taken towards the planet and x is the azimuthal direction, positive in the direction of the orbit. Flow particles have diameter d. A sketch of the simulation is given in Fig. 4.

Assuming frictionless surfaces, our contact forces are purely along the center-to-center line of colliding particles and the rotational degree of freedom is ignored. Defining the vector $\mathbf{g} \equiv \mathbf{c}_1 - \mathbf{c}_2$ as the relative velocity between a pair of particles, interactions are treated as instantaneous binary collisions, with energy dissipation modeled via a constant restitution coefficient, e:

$$g'_\beta k_\beta = -e g_\alpha k_\alpha, \tag{21}$$

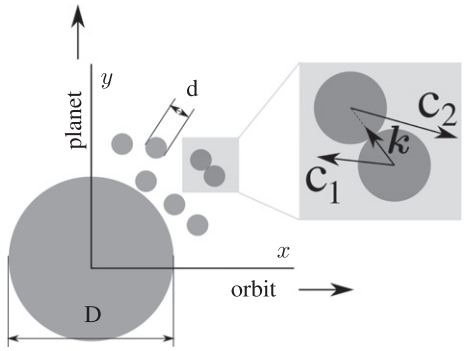

Fig. 4. Simulation layout. The inset shows a pair of flow particles with pre-collision velocities $\mathbf{c}_1$ and $\mathbf{c}_2$.

where the unit vector $\mathbf{k}$ defines the direction from the center of particle 1 to the center of particle 2 and the prime denotes a post-collision quantity. Vector components (denoted with Greek indices) are given with respect to a set of orthogonal basis vectors in the plane and we sum over a repeated index. The restitution coefficient ranges from 0 to 1, the latter corresponding to a perfectly elastic interaction. In combination with the linear momentum balance for identical particles, we can write the post-collisional velocities as

$$c'_{1\alpha} = c_{1\alpha} - \left(\frac{1+e}{2}\right) g_\beta k_\beta k_\alpha \tag{22}$$

and

$$c'_{2\alpha} = c_{2\alpha} + \left(\frac{1+e}{2}\right) g_\beta k_\beta k_\alpha. \tag{23}$$

The particle dynamics in our local reference frame (x,y) are governed by the homogeneous Hill equations (Murray and Dermott, 1999)

$$\frac{d^2y}{dt^2} + 2\Omega\frac{dx}{dt} - 3\Omega^2 y = 0 \tag{24}$$

and

$$\frac{d^2x}{dt^2} - 2\Omega\frac{dy}{dt} = 0, \tag{25}$$

where Ω is the orbital angular speed of the moonlet appropriate to its radial distance R, and is given by Newton's second law as $\Omega^2 = G_g m_s/R^3$ (gravitational constant G_g, mass of planet m_s). In the absence of gravitational forces from the moonlet, the equations are homogeneous.

We define dimensionless time $\tau^* \equiv \Omega t$ and scale all distances by the small particle's diameter $d(y^* = y/d, x^* = x/d)$ to obtain non-dimensional Hill equations,

$$\frac{d^2y^*}{d\tau^{*2}} + 2\frac{dx^*}{d\tau^*} - 3y^* = 0 \tag{26}$$

and

$$\frac{d^2x^*}{d\tau^{*2}} - 2\frac{dy^*}{d\tau^*} = 0. \tag{27}$$

The non-dimensional shear rate is $\dot\gamma^* = du^*/dy^* = 3/2$, where $u^* \equiv dx^*/d\tau^*$ is the non-dimensional speed in the azimuthal direction.

The simulation domain $(-w^*/2 \leqslant x^* \leqslant w^*/2,\ h^*/2 \leqslant y^* \leqslant h^*/2)$ makes use of the boundary conditions of Lees and Edwards (1972), which are periodic in the azimuthal direction, and incorporate appropriate transformations of position and velocity for periodicity in the radial direction,

$$\text{if } |y^*| > h^*/2: \quad y^*_\oplus = y^* \pm h^*, \quad u^*_\oplus = u^* \pm \dot\gamma^* h^*, \quad x^*_\oplus = x^* \pm \dot\gamma^* h^* \tau^*,$$

where the negative sign corresponds to particles exiting the top boundary and vice versa. The $\oplus$ subscript denotes the transformed position or speed. The Hill equations are invariant under such transformations of position and velocity (Wisdom and Tremaine, 1988) when particles cross the radial boundaries. The azimuthal extent of the simulation is taken to be large enough that apparent positional correlations/structure are destroyed by the shear flow and do not approach the boundaries. For our simulations we take $(w^*,h^*) = (2500,300)$, which creates a calculation domain that is approximately $125D^* \times 15D^*$, as our moonlets vary from $D^* = 10$ to $D^* = 30$, where $D^* = D/d$. For comparison, Lewis and Stewart (2009) employ a simulation domain that is ~500 times their moonlet diameter in the azimuthal direction and ~20 times larger in the radial direction. However, as noted in our discussion, their simulated propeller gap features are significantly longer in the azimuthal direction than those observed in our study. Additionally, we periodically circulate the particles by sampling from an unperturbed shear flow, in the spirit of Seiß et al. (2005), to minimize possible correlations that could persist across the periodic azimuthal boundaries.

Because of the scaling, control of the simulation is limited to the specification of scaled domain size (w^*,h^*), moonlet size D^*, restitution coefficient e, and global area fraction, ν. Particles are initially homogeneously distributed with a specified area fraction and are given azimuthal speeds appropriate for their radial distances from the moonlet, $u^* = \frac{3}{2}(y^* - h^*/2)$. After this, particle motions are governed by the Hill equations and collisional interactions with the moonlet and each other. Simulations are performed for increasing durations to ensure that a steady state has been reached. Typical simulation times correspond to $\sim 10^2$ orbits.

4. Results

Owing to the dissipative nature of the ring material (Goldreich and Tremaine, 1978; Hatzes et al., 1991; Supulver et al., 1995; Brilliantov et al., 1996; Porco et al., 2008, Fig. 14.3 in Schmidt et al. (2009)) and the flow conditions incident to the moonlet, the azimuthal speed in the shearing flow of Saturn's rings can be shown to be supersonic beyond several particle diameters of the moonlet's radial position. Since information about the presence of the moonlet cannot be transmitted upstream, shocks can develop.

We employ two-dimensional simulations to understand the effects of energy dissipation (the restitution coefficient), the collision frequency (area fraction), and the moonlet's relative size compared to the characteristic ring particle. In the following figures, only a portion of the entire simulation is pictured – the full simulation extends significantly further in both the radial and azimuthal directions. Simulation durations are on the order of 10^2 orbits, but we note that the propeller-like features are created and reach steady state far more rapidly. In one orbit, particles typically experience 15–100 collisions.

In Fig. 5, we vary the restitution coefficient and observe the change in both the detached shock feature and the vacancy downstream of the moonlet. Fig. 3 has demonstrated that the Mach number increases with decreasing restitution coefficient; in Fig. 5 we see the density in the shocked region is greater for more dissipative collisions, indicating a stronger shock. When particles are less elastic, smaller rebound speeds will occur, corresponding to decreased thermal/fluctuation velocities (or colder flows) and, thus, stronger shocks. It is also apparent that the more elastic collisions lead to a shorter vacant region downstream of the moonlet. Corresponding to the restitution coefficients of $e = 0.3, 0.5, 0.6, 0.8$ we measure azimuthal gaps of approximately $2.2D^*$, $2D^*$, $1.8D^*$, and D^*, respectively. This decrease in gap length is consistent with

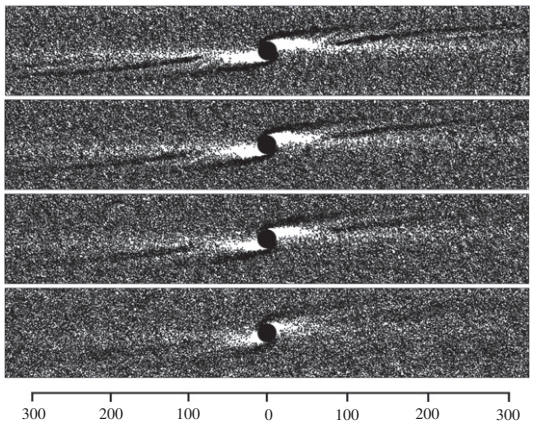

Fig. 5. Propeller formation for several different collisional restitution coefficients $e = 0.3, 0.5, 0.6, 0.8$ from top to bottom. In all cases here, the size ratio is $D^* = 25$ and the initial global area fraction is $\nu = 0.5$. Each image is plotted for a window of (700×120) small particle diameters.

the greater temperature that the more elastic particles possess. At the same packing fraction, the higher granular temperature results in increased collision frequency and a faster diffusion of particles into the vacancy. This suggests that the variation in the length of the empty region depends on factors other than the orbital dynamics (as described by the Hill equations); for example, collisional diffusion is likely to be relevant.

In Fig. 6, we vary the size of the moonlet relative to that of the small particles. We note that the resulting shock formations vary in size and intensity (density): for smaller moonlets ($D^* = 10$) only a very minimal shock forms and the global area fraction of the simulation is almost spatially uniform. For the larger size ratios, the shock does not begin at the orbital radius of the moonlet; the bottom of the shock, instead, starts several small particle diameters away from this line. Both of these observations suggest a threshold speed for shock creation, which we identify as the sound speed. The minimal shock for $D^* = 10$ indicates that incident shear flow is approximately sonic at no more than five particle diameters from the moonlet's semi-major axis. For the restitution coefficient of $e = 0.3$ and global area fraction of $\nu = 0.5$, Fig. 3 suggests that $M = 1$ occurs at approximately 2.5–3 particle diameters, which matches our simulations well.

Another striking feature of these images is the size of the vacant regions. Some studies (Seiß et al., 2005; Sremčević et al., 2007) suggest the azimuthal extent of these features is dependent on the Hill radius (where a moonlet's gravity is included), while others (Tiscareno et al., 2008) do not see this scaling. Since the moonlet has no gravitational effect on the particles in our model, the Hill radius – the region when a moon's gravity dominates the planet's (Murray and Dermott, 1999) – has no meaning. Nonetheless, it is clear that the body's size alone (without regard for its mass) has an appreciable effect on the resulting structure of the propeller. The vacant regions scale well with the moonlet size, with an approximate azimuthal extent of ≈2.0–2.2 moonlet diameters.

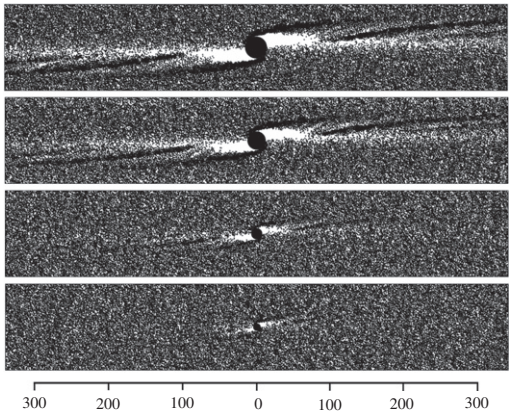

Fig. 6. Propeller formation for moonlet sizes $D^* = 30, 25, 15, 10$, from top to bottom. In all cases shown here, the restitution coefficient is $e = 0.3$ and the initial global area fraction is $\nu = 0.5$. Each image is plotted for a window of 700×120 small particle diameters.

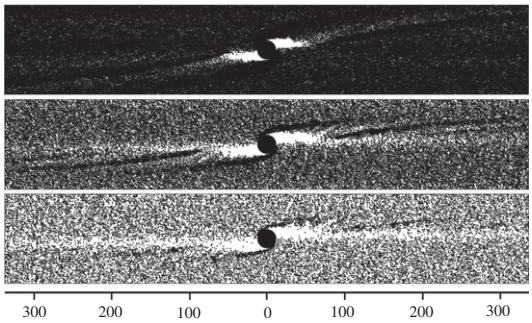

Fig. 7. Propeller formation for several different area fractions. From top to bottom: $\nu = 0.7, 0.5, 0.3$. In all cases shown here, coefficient of restitution is $e = 0.3$ and the size ratio is $D^* = 25$. Each image is plotted for a window of 700×120 small particle diameters.

Fig. 7 presents results from steady-state simulations for three values of global area fraction. We see shock formation in all three, as expected, but the width and shape of the shock vary significantly. As suggested by Fig. 3, we expect $M > 1$ beyond several particle diameters of the moonlet's axis for all of the densities shown. Even at the highest area fraction, we may still characterize the upstream flow as supersonic. The significant thickness and dark appearance of the shock in the top panel ($\nu = 0.7$) does not necessarily imply a stronger shock where the analysis predicts a lower Mach number; shock strength is characterized by the relative change in flow properties between the pre- and post-shock regions. We note that the lengths of the vacant regions decrease with increasing area fraction. We see that the denser situations exhibit shorter empty regions if a propeller is identified by the transmission (or reflection) of light relative to the surrounding ring material (Tiscareno et al., 2010). Although the increased density, in turn, lowers the velocity fluctuations, the collision frequency is higher and, hence, particles will diffuse faster into the empty region. As in the simulations where the restitution coefficient was varied, this emphasizes that the spatial extent of "propeller" features is not solely determined by the orbital dynamics, but collisional effects also have an influence.

Fig. 8 displays a portion of the top half of one of our simulations in order to illustrate the velocity field of the particles near the moonlet. This confirms that the shock is not a static aggregate of particles, but rather represents the locus of a continuing stream of particles past the moonlet. As the flow is abruptly turned by the body, it experiences changes in its properties. The shock's average spatial characteristics are steady in time, but there is a flux of mass entering and exiting the shocked region. A plot displaying the velocity field even closer to the moonlet (Fig. 9) reveals that particles in the shocked region have slowed as a result of mass and momentum considerations across the shock surface.

Our findings may be compared to those of Lewis and Stewart (2009), who include the moonlet's gravity; this allows some estimate of the relative importance of collisional and gravitational effects. In Lewis and Stewart's simulations, the moonlet's gravity has the effect of accreting flow particles on the body's perimeter and

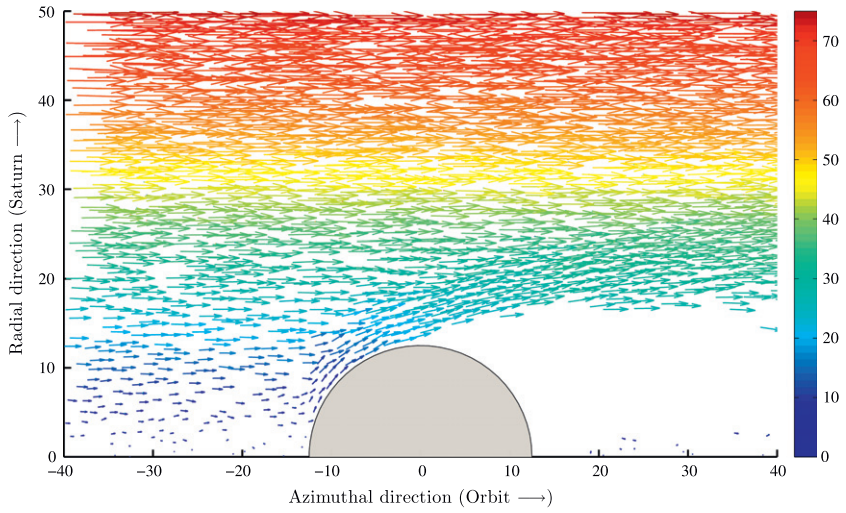

Fig. 8. The velocity field for a portion of the top half of a simulation with $D^* = 25$, $\nu = 0.5$, and $e = 0.3$. The colors and arrow lengths denote the non-dimensional velocity magnitude u^*. Scales on the respective axes denote the distance in small particle diameters. The collimated nature of the flow along the shock is apparent as is the incoming Kepler shear visible on the left edge (speeds are zero on the axis and increase linearly with distance off the axis). (For interpretation of the references to color in this figure legend, the reader is referred to the web version of this article.)

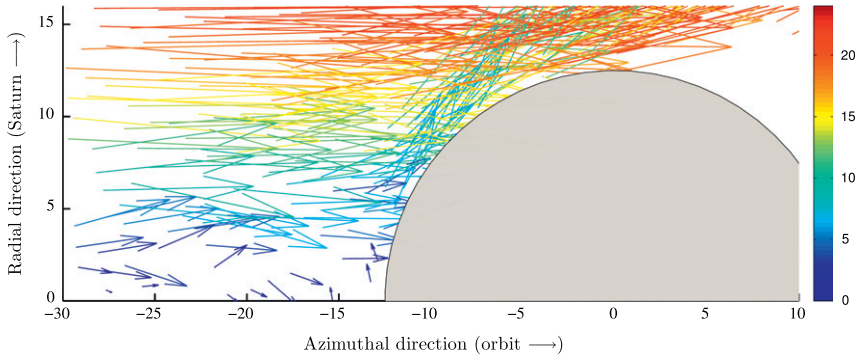

Fig. 9. A close-up of the velocity field plotted in Fig. 8. The colorbar and arrow lengths denote the non-dimensional velocity magnitude u^*. Scales on the respective axes denote the distance in small particle diameters. This clearly shows the slowing of the flow inside the shock local to the moonlet. (For interpretation of the references to color in this figure legend, the reader is referred to the web version of this article.)

also altering the shape and orientation of the high-density regions. We see that, with the inclusion of gravity, the high-density propeller feature is oriented in a more radial direction. Images (Lewis and Stewart, 2009) of particle clusters surrounding the moonlet show significant accretion on the "top" and "bottom" of the moonlet, depending upon the size ratios, particle size distribution, and self-gravitation. In contrast, our purely collisional simulation does not develop clumping and the particles comprising the shock feature do not remain attached to the moonlet. We do not believe that clustering precludes shock development, however. The size of the obstructing body is effectively expanded with gravitational accretion, but this may not appreciably change the upstream flow properties to prevent development of shocks. This needs future study.

In the gravitational simulations, the vacant regions are larger in both the radial and azimuthal directions. Collisional propellers, like ours, extinguish within several moonlet diameters whereas those including gravitation remain apparent for the entire azimuthal extent shown in Lewis and Stewart's images (see Fig. 4 in Lewis and Stewart (2009)). Until the size of the responsible moonlet and propellers is resolved from spacecraft images (or occultations), it will not be possible to determine the relative importance of the two effects. However, we recall that while the two-dimensional simulations show clear vacancies, the brighter regions appearing in the Cassini images are not necessarily empty regions. In fact, Tiscareno et al. (2008, 2010) indicate that the observed features in spacecraft images may, in fact, be due to local increases in the optical depth rather than mass density. The reader is directed to Sremčević et al. (2007) for discussion and modeling of the increase in optical depth. For the moment, we note that numerical simulations (with or without moonlet gravity) create visible gaps with bordering density increases (aggregation, shocks), and propeller observations are still subject to further interpretation as discussed by Tiscareno and co-workers (2010).

Secondary, high-density features border the vacant regions in simulations both with and without gravity. At significant distances from the moonlet where gravitational effects due to the moonlet are much less than that of the central planet, the creation of these structures may be determined solely by the dynamics that drive particle collisions. Indeed, collisional effects are, in part, responsible for some observed "wake" structures; inhomogeneous clustering has been observed in collisional flows for terrestrial applications. Hopkins and Louge (1991) quantified the microstructure created by inelastic shearing flows and their simulation images show very similar cluster features to the simulations of Lewis and Stewart (2009), in which self-gravity is included. We note that the findings of Hopkins and Louge (1991) contradict those of Salo (1995) and Daisaka and Ida (1999) who state that *both* inelasticity and self-gravitation are necessary for clustering.

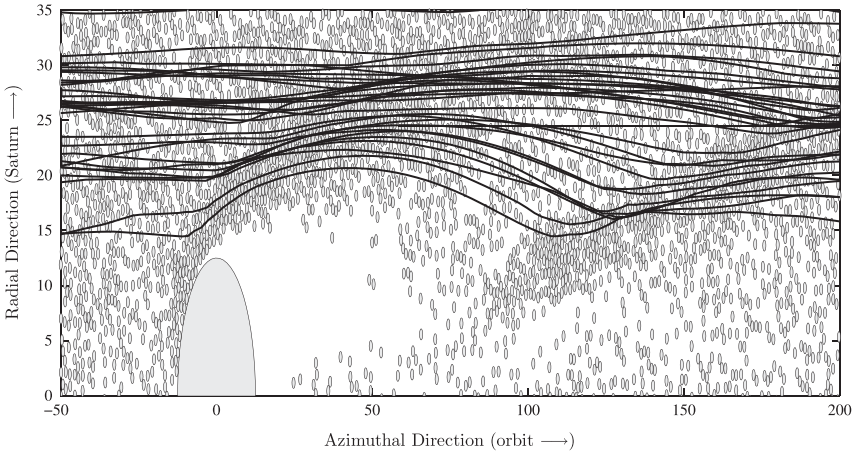

Fig. 10. Overlay of particle positions and trajectories of sample particles for a simulation (that shown in Fig. 5) with $D^* = 25$, $\nu = 0.5$, and $e = 0.3$. The figure's aspect ratio has been altered to allow for easier differentiation of particles and the trajectories. Scales on the respective axes denote distances in small particle diameters.

Moreover, shearing flows alone have been shown to lead to strong density concentrations in simulations with walls (Saitoh and Hayakawa, 2007) and with Lees–Edwards boundary conditions (Tan and Goldhirsch, 1997).

Fig. 10 displays particle positions with sample trajectories overlaid for a portion of the simulation shown in the top panel of Fig. 5. These trajectories display the epicyclic paths consistent with objects perturbed (in this case, by the moonlet and interparticle collisions) from their appropriate radial positions (cf. Fig. 3.30 in Murray and Dermott (1999)). Such epicycles are usually attributed to being initiated by the radial acceleration due to the moonlet's gravity (cf. Showalter and Burns, 1982), which is absent in our simulations. Instead, from our collisional simulations, we now recognize that the radial component of the rebound velocity caused by a collision will prompt such an oscillation just as effectively. The trajectories are observed to converge in the same region where the high-density structure is present. The higher density of particle paths suggests an increase in collision probability and this, of course, will lead to additional enhancement of the density structure through inelastic collisions which further augment the concentration of particles. The correlation of trajectories with these features suggests that the Hill equations dominate the formation of the secondary structures.

5. Summary and conclusions

We have examined formations reminiscent of propellers in Saturn's rings without invoking the moonlet's gravity, in the context of a granular shock. The effects of collisions, surface density, and moonlet size were qualitatively investigated with the use of two-dimensional discrete particle numerical simulations. Using an expression for the sound speed in classical thermodynamic equilibrium and the determination of the granular temperature in steady shear, we were able to estimate the nature of "cold", dissipative planar flows, which are assumed to be a simple representative model of Saturn's rings. Our analysis suggests that such flow is inherently supersonic and that granular shocks may play a role in propeller formation.

Our findings have similarities to aspects of simulations that include gravity, but some distinct differences also, namely, the azimuthal extent of low-density regions and the orientation and thickness of higher-density formations. However, without additional spacecraft observations at sufficient resolution, the details of the propeller gaps and adjacent density enhancements are not accessible. It remains to definitively quantify the relative importance of collisional effects and the gravitational forces. Inclusion of the moonlet's gravity introduces terms in the inhomogeneous Hill equations that depend on the moonlet's mass (see Section 9.5.3 in Murray and Dermott (1999); cf. Duncan et al., 1989); thus, such terms scale as the cube of the moonlet size and linearly with the mass density. Accompanying an increase in size or density, we expect the contribution of the gravitational terms to be increasingly significant. However, it may be that smaller or less dense moonlets exhibit behavior more consistent with that of a granular shock. Indeed, the shock conditions that we have studied may be relevant to the development and subsequent evolution of self-gravity wakes and clusters of gravitationally accreted particles (Schmidt et al., 2009).

Our heuristic two-dimensional simulation and analysis is intended to present a suggestive and, perhaps, predictive cartoon that collisional interactions alone are sufficient, but certainly not necessary, to explain the existence of propeller-like structures in a thin, dense ring. We accept that inhomogeneities in the concentration of ring particles that result from their gravitational interaction can influence the energy balance and can affect the determination of the granular temperature, and there certainly will be a change of thickness in the ring across the shock. However, we do not regard the existence of these structures nor the change in thickness as sufficiently important to invalidate our thesis that collisional interactions are responsible for some part of the morphology of propeller-like features.

Acknowledgments

The authors acknowledge helpful discussions with M.S. Tiscareno, M.M. Hedman, and J.N. Cuzzi as well as support from the Cassini project and NASA's Planetary Geology and Geophysics Program. Comments from two anonymous reviewers on an earlier draft have been instrumental in improving this manuscript.

References

Anderson, J., 2000. Hypersonic and High Temperature Gas Dynamics. AIAA.
Brilliantov, N., Spahn, F., Hertzsch, J., Pöschel, T., 1996. A model for collisions in granular gases. Phys. Rev. E 55, 5382–5392.
Charnoz, S., Dones, L., Esposito, L., Estrada, P., Hedman, M., 2009. Origin and evolution of Saturn's ring system. In: Dougherty, M., Esposito, L., Krimigis, S. (Eds.), Saturn from Cassini–Huygens. Springer, Dordrecht, pp. 537–575.
Cuzzi, J. et al., 2009. Ring particle composition and size distribution. In: Dougherty, M., Esposito, L., Krimigis, S. (Eds.), Saturn from Cassini–Huygens. Springer, Dordrecht, pp. 459–512.
Cuzzi, J., Burns, J., Durisen, R., Hamill, P., 1979. The vertical structure and thickness of Saturn's rings. Nature 281, 202–204.

Cuzzi, J. et al., 2010. An evolving view of Saturn's dynamic rings. Science 327, 1470–1475.
Daisaka, H., Ida, S., 1999. Spatial structure and coherent motion in dense planetary rings induced by self-gravitational instability. Earth Planet Sci. 51, 1195–1213.
Duncan, M., Quinn, T., Tremaine, S., 1989. The long-term evolution of orbits in the Solar System: A mapping approach. Icarus 82, 402–418.
Goldreich, P., Tremaine, S., 1978. The velocity dispersion in Saturn's rings. Icarus 34, 227–239.
Gray, J., Cui, X., 2007. Weak, strong and detached oblique shocks in gravity-driven granular free-surface flows. J. Fluid Mech. 579, 113–136.
Haff, P., 1983. Grain flow as a fluid-mechanical phenomenon. J. Fluid Mech. 134, 401–430.
Hatzes, A.P., Bridges, F., Lin, D., Sachtjen, S., 1991. Coagulation of particles in Saturn's rings – Measurements of the cohesive force of water frost. Icarus 89, 113–121.
Hopkins, M., Louge, M., 1991. Inelastic microstructure in rapid granular flows of smooth disks. Phys. Fluids A 3 (1), 47–57.
Jenkins, J., Richman, M., 1985. Kinetic theory for plane flows of a dense gas of identical, rough, inelastic, circular disks. Phys. Fluids 28, 3485–3494.
Jenkins, J., Richman, M., 1988. Plane simple shear of smooth inelastic circular disks: The anisotropy of the second moment in the dilute and dense limits. J. Fluid Mech. 192, 313–328.
Lees, A., Edwards, S., 1972. The computer study of transport processes under extreme conditions. J. Phys. C 5, 1921–1929.
Lewis, M., Stewart, G., 2009. Features around embedded moonlets in Saturn's rings: The role of self-gravity and particle size distributions. Icarus 199, 387–412.
Michikoshi, S., Kokubo, E., 2011. Formation of a propeller structure by a moonlet in a dense planetary ring. Astrophys. J. 732, L23–L26.
Murray, C., Dermott, S., 1999. Solar System Dynamics. Cambridge University Press.
Porco, C., Weiss, J., Richardson, D., Dones, L., Quinn, T., Throop, H., 2008. Simulation of the dynamical and light scattering behavior of Saturn's rings and the derivation of ring particle and disk properties. Astron. J. 136, 2172–2200.
Rericha, E., Bizon, C., Shattuck, M., Swinney, H., 2002. Shocks in supersonic sand. Phys. Rev. Lett. 88, 014302.
Saitoh, K., Hayakawa, H., 2007. Rheology of a granular gas under a plane shear. Phys. Rev. E 75, 021302.
Salo, H., 1995. Simulations of dense planetary rings – III: Self-gravitating identical particles. Icarus 117, 287–312.
Schmidt, J., Ohtsuki, K., Rappaport, N., Salo, H., Spahn, F., 2009. Dynamics of Saturn's dense rings. In: Dougherty, M., Esposito, L., Krimigis, S. (Eds.), Saturn from Cassini–Huygens. Springer, Dordrecht, pp. 413–458.
Seiß, M., Spahn, F., Sremčević, M., Salo, H., 2005. Structures induced by small moonlets in Saturn's rings: Implications for the Cassini mission. Geophys. Res. Lett. 32, L11205.
Showalter, M., Burns, J., 1982. A numerical study of Saturn's F ring. Icarus 52, 526–544.
Spahn, F., Sremčević, M., 2000. Density patterns induced by small moonlets in Saturn's rings? Astron. Astrophys. 358, 368–372.
Sremčević, M., Spahn, F., Duschl, W., 2002. Density structures in perturbed thin cold discs. Mon. Not. R. Astron. Soc. 337, 1139–1152.
Sremčević, M., Schmidt, J., Salo, H., Seiß, M., Spahn, F., Albers, N., 2007. A belt of moonlets in Saturn's A ring. Nature 449, 1019–1021.
Sremčević, M., Stewart, G., Albers, N., Esposito, L.W., 2011. Discovery of B-ring propellers in Cassini UVIS and ISS. 2011AGUFM. P13B16775.
Supulver, K., Bridges, F., Tiscareno, S., Lievore, J., Lin, D., 1995. The coefficient of restitution of ice particles in glancing collisions: Experimental results for unfrosted surfaces. Icarus 129, 539–554.
Tan, M., Goldhirsch, I., 1997. Intercluster interactions in rapid granular shear flows. Phys. Fluids 9 (4), 856–869.
Tiscareno, M. et al., 2006. 100-metre-diameter moonlets in Saturn's A ring from observations of 'propeller' structures. Nature 440, 648–650.
Tiscareno, M., Burns, J., Hedman, M., Porco, C., 2008. The population of propellers in Saturn's A ring. Astron. J. 135, 1083–1091.
Tiscareno, M. et al., 2010. An analytic parameterization of self-gravity wakes in Saturn's rings, with application to occultations and propellers. Astron. J. 139, 492–503.
Verlet, L., Levesque, D., 1982. Integral equations for classical fluids III. The hard discs system. Mol. Phys. 46, 969–980.
Walton, O., Braun, R., 1986. Viscosity, granular-temperature, and stress calculations for shearing assemblies of inelastic, frictional disks. J. Rheol. 30 (5), 949–980.
Wisdom, J., Tremaine, S., 1988. Local simulations of planetary rings. Astron. J. 995, 925–940.
Zebker, H., Marouf, E., Tyler, G., 1985. Saturn's rings: Particle size distributions for thin layer models. Icarus 64, 531–548.